INS-NUMA-24

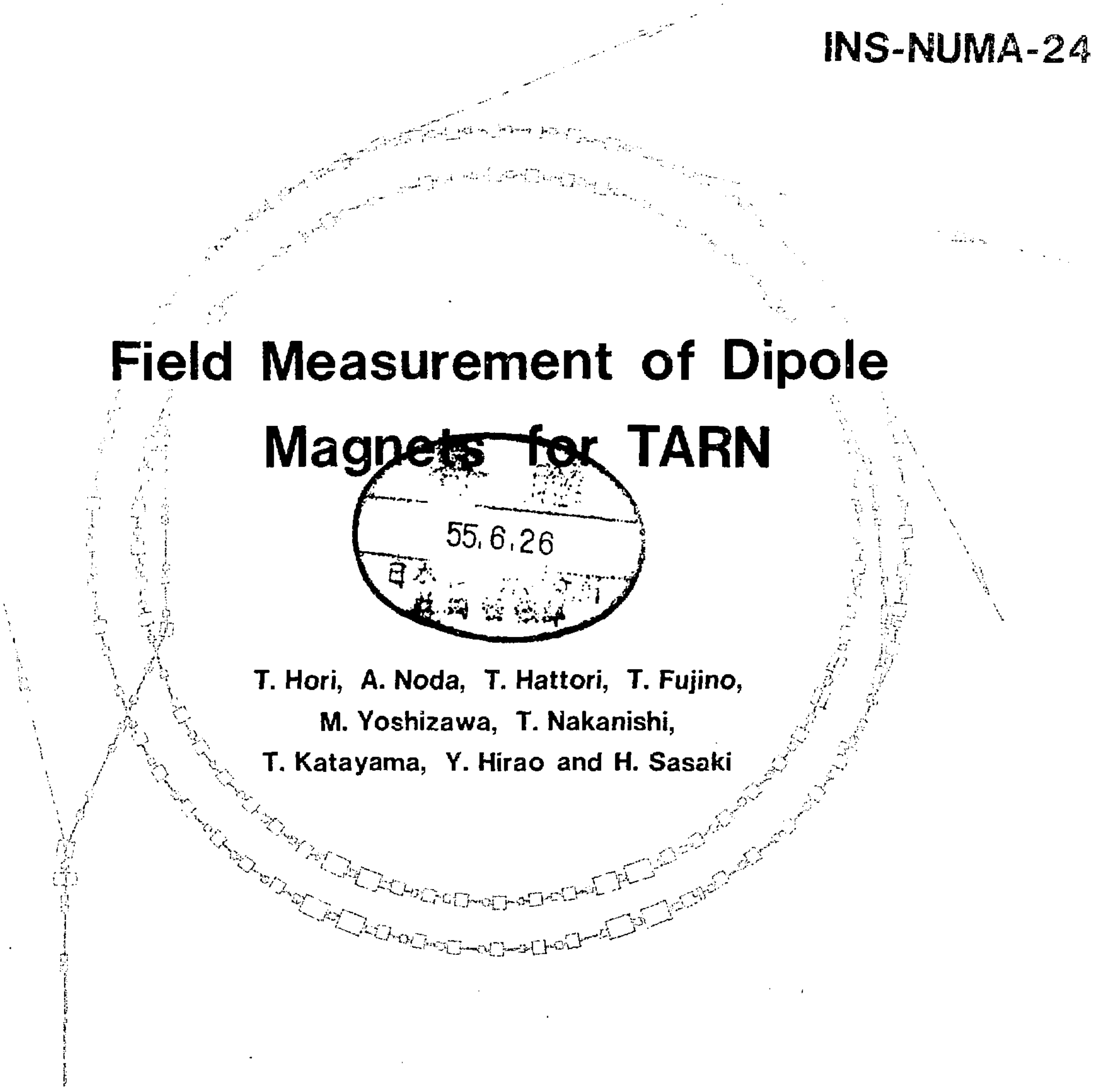

Field Measurement of Dipole Magnets for TARN

T. Hori, A. Noda, T. Hattori, T. Fujino,
M. Yoshizawa, T. Nakanishi,
T. Katayama, Y. Hirao and H. Sasaki

May 1980

STUDY GROUP OF NUMATRON AND
HIGH-ENERGY HEAVY-ION PHYSICS
INSTITUTE FOR NUCLEAR STUDY
UNIVERSITY OF TOKYO
Midori-Cho 3-2-1, Tanashi-Shi,
Tokyo 188, Japan

Field Measurement of Dipole Magnets for TARN

T. Hori*, A. Noda, T. Hattori, T. Fujino, M. Yoshizawa,
T. Nakanishi, T. Katayama, Y. Hirao and H. Sasaki**

Institute for Nuclear Study, University of Tokyo

Abstract

Eight dipole magnets of window-frame type with zero field gradient have been fabricated for TARN. Various characteristics of the field were examined by a measuring system with a Hall and an NMR probes. The accuracy of the measurement was better than 1×10^{-4} at the maximum field strength of ~ 9 kG, and the uniformity of the field in the radial direction was better than $\pm 2 \times 10^{-4}$ over the whole useful aperture. The deviations both of the field strengths and of the effective lengths among the eight magnets are smaller than $\pm 2 \times 10^{-3}$. The sextupole component of the field and the variation of the effective length over the beam orbits contribute to chromaticities of the ring as the amount of -1.59 and 0.93 in the horizontal and vertical directions, respectively.

---

* On leave from Sumitomo Heavy Industries, Co. Ltd.

** National Laboratory for High Energy Physics (KEK).

1. Introduction

A storage ring of heavy ions named TARN (Test Accumulation Ring for NUMATRON project) is designed and constructed with a separated function $\bar{F}O\bar{D}O$ lattice[1]. It aims at the accumulation of heavy ions such as N^{5+} with a kinetic energy of 8.5 MeV per nucleon injected from the SF cyclotron. An overall view of the completed TARN is shown in Fig. 1.

The ring has eight periods and in each cell one dipole magnet is placed, whose bending angle is 45 degrees. The structure of a normal cell is shown in Fig. 2. The beam orbit is calculated by the computer code SYNCH[2]. The number of betatron oscillations per revolution is around 2.25 both in horizontal and vertical directions. The orbit characteristics are given in Fig. 3, where beta functions, their derivatives and dispersion function are illustrated. Using the results of analysis, the aperture of the dipole magnet is determined. In Table 1, the aperture requirement for the dipole magnet is given and is illustrated in Fig. 4. Considering the space necessary for the installation of distributed ion pumps and heat insulation materials for baking, we decided the gap of the magnet to be 70 mm and the width of the magnet aperture to be 258 mm.

Among the values of radius of curvature ρ, length of the dipole magnet L_B and the number of dipole magnets N_B, the following relation should exist

$$N_B L_B = 2\pi\rho \quad . \tag{1}$$

In the present case, N_B and L_B are 8 and 1.047 m, respectively, and ρ is 1.333 m. Due to the rather small radius of curvature, the so-called sagitta d_s, which can be calculated by the relation

$$d_s = \frac{L_B^2}{16\rho} \quad , \tag{2}$$

amounts to such a value of 5.1 cm if we make the dipole with a straight rectangular magnet. Therefore, the dipole magnet for TARN is decided to be fan-shaped and has normal entrance and exit.

After the fabrication of magnets, the field properties are studied by the measuring system with a Hall-probe of which the position is controlled by a mini-computer system. In the present paper, the design principle of the dipole magnet and the method of field measurement are described in chapters 2 and 3, respectively. The measured results of the magnetic field and its analysis are described in chapter 4, and the effects of the field on the beam dynamics are briefly given in chapter 5.

2. Construction of Dipole Magnets

2-1. Basic Principle

In the design of a bending magnet, several types of structure are considered, i.e. window-frame type, C-type and H-type. The window-frame type magnet has uniform magnetic field with a simple structure to fabricate. On the assumption that iron has the infinite permeability, the vertical component of the magnetic field, B_z, is essentially uniform in the full aperture.

The H-type magnet requires rather complicated pole shape to attain good field property and becomes larger than window-frame type in order to obtain the same good field region. This type has an advantage that the coils can be made as simple pancakes which need not be bent at the ends of the magnet. On the contrary, the coils of window-frame type should be bent so as to keep a passage of beam. It requires a little complicated fabrication process of coils, but the space can be saved in the direction of a beam path by bending up and down the coils. This is one of the reasons why the window-frame type is employed for the present case. The required space for our magnets outside the magnet edge is only 95 mm including a field clamp.

The most useful advantage of a C-magnet is its easy access to the vacuum chamber. But the C-magnet can be thought as an H-magnet with one backleg removed, therefore, it needs to be made larger and has the same disadvantage as that of H-type.

The modified window-frame magnet is a hybrid between window-frame type and H-type. It is not so simple as window-frame type but can provide the good field uniformity. Wide space outside the magnet edge must be taken into account in this type compared with window-frame type, for the coils thicker than the gap height are bent up and down. Considering the various properties of these types, we adopted finally the window-frame type magnet because of its good field property and compactness.

2-2. Design of the dipole Magnets for TARN

A. Field Strength

From the SF cyclotron with K number of 67, a beam of N^{5+} with the kinetic energy of 8.55 MeV/u are provided for TARN. The magnetic rigidity of the beam at injection is represented by

$$B\rho[\mathrm{kG\cdot cm}] = \frac{1}{0.3\varepsilon}\sqrt{T_N^2 + 2E_oT_N} \quad , \qquad (3)$$

where B[kG] is the flux density at the magnet gap, ε is charge to mass ratio, T_N[MeV/u] and E_o[MeV/u] are kinetic energy per nucleon and atomic mass unit, respectively. In the present case, with values of $\varepsilon(0.357)$ and E_o(931.5 MeV/u) it results in

$$B\rho = 1180 \quad \mathrm{kG\cdot cm} \quad . \tag{3'}$$

The radius of injection orbit ρ_{inj} is obtained from the momentum difference between a central and an injection orbits as follows,

$$\frac{\rho_{inj}}{\rho_c} = \frac{P_{inj}}{P_c} = 1 + \frac{\Delta P_{inj}}{P_c} \quad , \tag{4}$$

where $\Delta P_{inj}/P_c$ was designed as 3.14%[3)] and the radius of central orbit ρ_c is 1333 mm, thus, ρ_{inj} is 1375 mm. From the relation (3'), the required field B is 8.583 kG.

The necessary Ampère-turn to realize the above field is calculated by

$$NI = \frac{B_g d}{\mu_o} + \frac{B_i \ell}{\mu_i} \quad , \tag{5}$$

where B_g and B_i are the magnetic flux densities in the air gap and in the iron yoke, respectively, d is the gap height, ℓ is the path length of magnetic flux in the yoke, μ_i and μ_o are the permeabilities of the iron and the air, respectively. If the effect of saturation in the iron is negligible, the equation (5) can be simplified as

$$NI \simeq \frac{B_g d}{\mu_o} \tag{5'}$$

and NI becomes 50100 AT for the values of B_g(0.9 Tesla), d(0.07 m) and μ_o($4\pi \times 10^{-7}$ H/m). The computer program TRIM[4),5)] was used to study more accurately the required Ampère-turn and the field property in the gap. The result is almost the same with the above value. The design value is decided to be 55200 AT including a margin to afford additional magnetic motive force which cannot be taken into account at the calculation of TRIM. The field distribution in the aperture in radial direction was obtained by the cylindrical model calculation[6)] and the result is given in Fig. 5 with an example of measured data.

B. Specifications

The poles and yokes are made of low carbon steel and its chemical components are listed in Table 2. The B-H characteristics of the material was studied with samples from the raw steel blocks. (Fig. 6) The calculation by TRIM shows that B_i is less than 1.7 T in almost all the region of the poles and yokes. When we assume the average flux density $\overline{B}_i$ as 1.6 T and the average path length $\overline{\ell}$ as 1.5 m, the average permeability $\overline{\mu}_i/\mu_o$ should be larger than 560 from the equation (5). On the other hand, Fig. 6 shows that the value of H is 1800 A/m when B_i is 1.6 T and $\overline{\mu}_i$ is also estimated at 700 from the relation

$$\frac{\mu_i}{\mu_o} = \frac{B}{H} \quad . \tag{6}$$

For the fabrication of the magnets, we decided to make the magnet as compact as possible with using the iron which is a little saturated but field properties would not be so largely affected. An empirical equation is given[7)] as follows, which gives the sextupole component of window-frame type magnet,

$$\frac{1}{2B_o}\frac{d^2B}{dr^2} = 0.2 \left(\mu_i \frac{d}{2} \frac{w_a + w_c}{2}\right)^{-1} \quad , \tag{7}$$

where w_a and w_c are widths of the aperture and the coil region, respectively. From the values of w_a(0.258 m), w_c(0.323 m) and μ_i, $\frac{1}{B_o}\frac{d^2B}{dr^2}$ is estimated at 0.056 ∿ 0.070 m^{-2}. It agreed well with the measured value and, to be described later, has minor influence on beam dynamics. It is known from Fig. 5 that the uniformity of the field is better than 6×10^{-4} even for this compact magnet.

The corners of the magnet edge are cut off with four steps (Fig. 7) so as that its shape is close to the Rogowski's curve[8)] which is represented as

$$\frac{z}{d/2} = 1 + \frac{2}{\pi}\exp\left(\frac{\pi}{2}\,\frac{y}{d/2}\right) \quad , \tag{8}$$

where the (y, z) co-ordinate system is illustrated in Fig. 7. By the use of this edge-shape, we obtain the constant structure of fringing field[9)] for the various field strengths, which is preferable as we intend to accumulate ions of various energies. The shielding plates, called field clamps, are utilized to fix the distribution curves of fringing field and to cut off the tail of the fringing field before the adjacent quadrupole magnets.

The specifications of the dipole magnet are listed in Table 3. The inductance L of main coils is estimated by the following relation,

$$L = N^2 \frac{\mu_o}{d} A_g \quad , \tag{8}$$

where N is the number of turns and A_g is effective area in which the total flux ϕ is passing through with the density B_g. Therefore, A_g is represented as

$$A_g = \rho \cdot \theta \cdot (w_a + w_c) \quad , \tag{9}$$

where ρ and θ are the radius at the center of the aperture and the bending angle, respectively. The inductance L is 200 mH in the case ρ is 1.353 m and θ is $\pi/4$ rad.

By the correction coils of 600 AT, the tunable range of $\frac{\Delta B}{B} = \pm 5 \times 10^{-3}$ is provided to adjust the deviation of each magnet. The use of correction coils reduced a degree of requirement for the tolerance of each magnet. The manufacturing accuracy was aimed at within ±0.1 mm for the designed gap height of 70 mm, which is rather easy specification as a result of the attachment of the correction coils. The accuracy of flatness of the magnet gap was required to be less than 50 μm in whole aperture and the observed values are found to be better than the designed value.

The plan and cross sectional views of the magnet are illustrated in Fig. 8 and the total view of the manufactured magnet is shown in Fig. 9.

3. Field Measurement

Magnetic field properties such as excitation characteristics, radial dependence of the field, the length of effective field and its radial dependence are studied in detail as well as individualities of the magnets. The end field of dipole magnet was measured with a Hall-probe because of its simplicity and sufficient resolusion, while another method such as flip coils measurement had been considered.

3-1. Measurement System

The block diagram of the automatic control system is shown in Fig. 10, which consists of two parts, one is to drive a Hall-probe in a horizontal plane and the other is to take in measured data (Fig. 10-a). A mini-computer HP-1000 system is used as a controller, together with some peripherals (Fig. 10-b).

The measurement items are as follows.

(1) (x, y) coordinate in the plane — information of position,

(2) output voltage of Hall probe,

(3) frequency of proton NMR probe — as a monitor of the inner field,

(4) shunt voltage of a current source.

As suggested in Figs. 10-a and 11, the instruction of the first item is generated in the computer, and the driving system positions the probe and the setting accuracy is checked. After the measurement is performed, the data of items no. 2 and 4 are sent to CPU from the digital voltmeter through GP-IB line. At the same time the item no. 3 is also sent to CPU from a frequency counter through a microcircuit interface. These data are temporarily accumulated in the CPU memory and the piled data are stored in a disk cartridge when the data corresponding to one line along y-direction are collected. The data are written with double precision format so as to keep sufficient significant figures of digits in the fractional part of numerical values and to maintain its preciseness after the completiton of analysis.

The driving apparatus, details of which are described in the next section, can move a probe along two directions orthogonal to each other in a horizontal plane, therefore, it covers a rectangular area (Fig. 12). The longer axis of the rectangle is always set normal to a magnet edge. The size of mapping area is 68 × 20 cm^2 in ordinary case. The intervals of mesh points along y- and x-direction are 5 mm and 10 mm (sometimes 5 mm used to fine mesh), respectively. The number of measured point, therefore, amounts to 2800 and the mesh density is 2 points/cm^2. It takes 2 sec/piont and 2 hours/run by the use of the automatic measuring system.

3-2. Driving Mechanism

The whole view of measuring system is shown in Fig. 13. A Hall-probe is positioned automatically by the driving system in the horizontal plane while manually in the vertical direction. There are two pulse motors in the driving mechanism which receive instruction pulse signals from HP-1000 via the pulse motor controller[10]. The torque of motors is transmitted through ball screw shaft connected directly to an axis of the pulse motor.

A Hall-probe contained in a copper box is fixed at an end of a 80 cm long SUS 316L pipe, which is supported tightly with the stand at the other end. The grip of the stand is movable vertically to adjust the level of the probe. The spans of the driving apparatus in the x-, y- and z-direction are as follows:

(1) 70 cm for y-dirction.

This span almost covers the extent between 30 cm outer point from a field clamp and 20 cm inner one from the end of Rogowski's cut. In case that the more inner/outer zone should be measured, a mapping area can be shifted with ease by changing the relative position of a probe in the apparatus. Normaly it covers the necessary range to get data, where the relative field strength in that extent varies from 0.2 % to 100 % compared with fully inner field.

(2) 40 cm for x-direction.

The direction is parallel to the magnet edge. The span covers whole width of the aperture (25.8 cm) in the magnet.

(3) 10 cm for z-direction.

The adjustable range of level is wide enough compared with the magnet gap height of 7 cm. In the performance of the measurement, the used span is ±15 mm from the median plane.

The resolution of pulse motors is 25 μm/pulse and motors are used only uni-directionally to avoid the backlashes of them. The driving apparatus monitors a position of a Hall-probe by rotary encoders. According to a movement of the probe, the rotary encoder generates pulses corresponding to the displacement of the probe. The system always checks the consistency of displacements by comparing the pulse number sent to a pulse motor with that received from a rotary encoder. The operator receives a warning when the difference of both pulse numbers exceeds an allowable value. It is found that the accuracy of the driving system is enough satisfactory, namely, the deviation is less than ±0.1 mm for twenty times of reversible motions in 700 mm span.

3-3. Hall Probe

A Hall-probe (Siemens FC33) has a size of 3 × 6 mm^2. The temperature coefficient of the probe is -0.04 %/ degree between -40°C and 80°C. It is essential to control a temperature of Hall-probe as we intend to get the measuring accuracy of 10^{-4}, namely, the fluctuation of the probe's output should be less than 1×10^{-4} which corresponds to the temperature variation of 0.25°C. A probe and a high quality thermistor as a temperature sensor are stored in a 30 × 15 × 10 mm^3 copper thermostatic oven together with heaters. They are wrapped by thermal insulaters and set in a container of 40 × 25 × 14.5 mm^3 copper box. The feedback circuit in temperature control system11) is shown in Fig. 14-a. It keeps the oven constant at about 50°C within the fluctuation of ±0.1°C.

Stabilization of a current source of probe is important as well as temperature control, which is performed by the D.C. current stabilizing circuit11) shown in Fig. 14-b. The output current is about 50 mA and its fluctuation is the order of 10^{-6}, which is attained by the use of highly accurate resistances and the temperature contol of them by taking in a double shielded oven. The temperature in the oven is kept at about 45°C within the fluctuation of ±0.2°C.

The sensitivity of the probe (flux density per output voltage) is about 140 Gauss/mV. On the other hand, the maximum resolution of the digital voltmeter (HP 3455A) is 1 μV, therefore, the resolution of the system is 0.14 Gauss. According to the specification of the digital voltmeter, the fluctuation is ± 0.003 % of the indicated value plus 4 digits within 24 hours and in the atmosphere of (23 ± 1)°C. Therefore fluctuation of the digital voltmeter amounts to around 6 μV at the maximum field (∿9 kG) and we can get the precision better than 1 Gauss.

3-4. System Stability

Preceding the measurement, it was carried out to check up the stabilities both of the Hall-probe and of the power supply for magnets. The stability of the measuring system including the Hall-probe and the digital voltmeter is shown in Fig. 15, where the rate of data taking was 20 per minute. It is shown in the figure that about a few hours later than the system-on, the stability becomes completely within the fluctuation of the digital voltmeter.

The stability of the current source of the magnets at I = 400 A is about 0.3×10^{-4} and the stability of the measuring system is within 0.7×10^{-4} which is almost due to the fluctuation of the digital voltmeter. The output voltage of the Hall-probe is almost proportional to the field strength and its calibration curve is fitted with fourth order polynominal

(Fig. 16). Numerical values of first and second order terms are 0.14 ∿ 0.15 kG/mV and -0.0062 kG/mV^2, respectively.

We are not anxious about instability of the power supply by reason that the fast components of its fluctuation cannot affect the field strength because of the long time constant of the magnet which is estimated at 1.4 sec from the values L and R of the main coil. On the other hand, slow variations of the source current are compensated by means of normalization of the Hall-probe's output with the central field strength detected by NMR, the frequency of which has an accuracy better than 10^{-5}.

4. Results

The magnetic field of all the eight magnets was measured and these data were analyzed by the use of the mini-computer HP1000. The (r, s) co-ordinates system shown in Fig. 12 is used in analyses. The values necessary to discuss beam properties are all collected in tables.

(1) Excitation

The measured excitation characteristics of the magnets are shown in Fig. 17, where the magnetic field measured with NMR is given against the excitation current. At the same time, we also measured the output voltage of the Hall-probe and obtained the calibration curve of probe. The relation between magnetic field and excitation current shows a little tendency of saturation above 300 A, and it becomes much obvious in the relation between B/I and I. The tendency of saturation has no noticeable effect on the field properties as described later. It is found from the figure that the maximum field strength of our interest, 8.58 kGauss, is produced by the excitation current of 375 A.

The dipole magnets are used only by direct current and, therefore, the problem of hysteresis is not so troublesome. The method to monitor field by NMR excludes ambiguity due to hysteresis. The measurement of excitation curve for increasing or decreasing currents shows the hysteresis characteristics as given in Fig. 18.

The excitation curves of the eight magnets are fitted to fifth order polynominals where the error of fitting is minimum and the coefficients of polynominal are listed in Table 4.

(2) Fringing Field

A typical example of the measured fringing fields is shown in Fig. 19 along the central orbit with the radius of 1.333 m. The extension of the fringing field is well suppressed by the field clamp at the expense of a small amount of the central field strength (≃ 1.7 % at I = 400 A). There had been an conception that eight iron bolts, with which the clamps are fixed to the side yokes, play some roles in streaming of a part of the flux through the clamps. The fringing field near the clamps was measured on the two conditions, one is the case used ordinary iron bolts and the other SUS 304 bolts, and there was no detectable difference in the field strength between them.

The z-component of normalized fringing field is represented by polynominal expansion as

$$
\begin{aligned}
B_{\mathrm{fring}}(s)/B_0 &= \frac{1}{B_0}\left[B(0) + B'(0)\cdot s + \frac{1}{2}B''(0)\cdot s^2 + \ldots.\right] \\
&= \sum_{n=0}^{N} \frac{1}{n!} a_n s^n \quad , \qquad (10) \\
a_n &= B^{(n)}_{\mathrm{fring}}(0)/B_0 \quad ,
\end{aligned}
$$

where the origin of s co-ordinate is the edge of the magnet and B_0 equals to the central field strength. The expansion up to the seventh order is needed to fit the measured result reasonably within the range of $-120\ \mathrm{mm} \leq s \leq 120\ \mathrm{mm}$. The coefficients a_n are obtained and listed in Table 5 in which various cases are shown, e.g. current dependence, z-dependence etc. The three dimensional edge field distribution is easily reproduced from the values in the table.

(3) Effective Length

The definition of effective length is given by

$$L_{eff}(r) \equiv \int_{-\infty}^{\infty} B(s,\ r)/B_0\, ds \quad . \tag{11}$$

In our case, effective length ℓ_{eff} is obtained from the equation (11) by defining the integral region,

$$\ell_{eff}(r) = \int_{s_1}^{s_2} B(s,\ r)/B_0\, ds \quad , \tag{11'}$$

where s_1 and s_2 represent the points inner enough in the magnet gap (about 27 cm inside from the mechanical edge) and 40 cm outer from the edge in which $B(s)/B_0$ are 1.0 and 2×10^{-3}, respectively. The $\Delta\ell_{eff}(r)$ which is shown in Fig. 20 for the excitation currents of 200 A and 400 A are defined by the following relation.

$$\Delta\ell_{eff}(r) = \ell_{eff}(r) - \ell_{geom} \quad , \tag{12}$$

where ℓ_{geom} denotes the length from s_1 to the geometrical edge point (see Fig. 12). That is to say, $\Delta\ell_{eff}(r)$ represents the difference of actual magnetic length from the geometrical one.

The best fit approximation was applied to $\Delta\ell_{eff}(r)$ in the region of $-85\ \mathrm{mm} \leq r \leq 85\ \mathrm{mm}$, where the origin of r-axis is the middle point between two coils ($\rho = 1353$ mm) and it is 20 mm outer side from the central orbit. From the equation

$$\Delta\ell_{eff}(r)/\ell_g(r) = \frac{1}{\ell_g(r)}\left[\ell_{eff}(0)-\ell_g(0)+\ell'_{eff}(0)\cdot r+\frac{1}{2}\ell''_{eff}(0)\cdot r^2+\ldots\right]$$
$$= \sum_{n=0}^{N} \frac{1}{n!} b_n r^n \quad , \qquad (13)$$

where $\ell_g(r)$ means the total geometrical length of one magnet, 1063 mm at $r = 0$, and the coefficients b_n are represented as

$$\begin{aligned} b_0 &= (\ell_{eff}(0) - \ell_g(0))/\ell_g(r) \qquad (n=0) \quad , \\ b_n &= \ell^{(n)}_{eff}(0)/\ell_g(r) \qquad (n \geq 1) \quad . \end{aligned} \qquad (14)$$

The coefficients b_n (up to $n = 4$) at $r = 0$ are listed in Table 6 for all the magnets.

The effect of field clamps appears most apparently in the fact that the factor $b_2[=\ell''_{eff}(0)/\ell_g(r)]$, which is the main part of the sextupole component as proved soon later, was reduced from $\sim -0.4\ \mathrm{m}^{-2}$(clamps off) to $\sim -0.1\ \mathrm{m}^{-2}$(clamps on).

(4) Uniformity

The uniformity of field at the inner position of the gap was investigated along the radial direction. The radial distribution of magnetic field or its difference from the value at $r = 0$, is shown in Fig. 21, where $\Delta B(r)$ (= $B(r) - B(0)$)is normalized by the central field strength B_0 measured with NMR probe. The saturation effect appears little in the difference of the $\Delta B(r)$ distribution at $I = 400$ A and 200 A, and it causes the disturbance of uniformity less than 1×10^{-4}. Having made the best fit approximation, the coefficients c_n are calculated and listed in Table 7, where the relation between c_n and $B(r)$ is as follows:

$$\begin{aligned} \Delta B(r)/B_0 &= \frac{1}{B_0}[B(0)-B_0+B'(0)\cdot r + \frac{1}{2}B''(0)\cdot r^2 + \ldots.] \\ &= \sum_{n=0}^{N} \frac{1}{n!} c_n r^n \quad , \\ c_0 &= (B(0) - B_0)/B_0 \qquad (n=0) \quad , \\ c_n &= B^{(n)}(0)/B_0 \qquad (n\geq 1) \quad . \end{aligned} \tag{15}$$

The coefficient c_0 represents the difference of the field strength between at the point of $r = 0$ ($B(0)$) and at the point NMR probe placed (B_0), but it is not the matter of our concern by reason of no influence upon beam property. The deviation of $|B(r)/B_0|$ is less than 2×10^{-4} within the useful aperture of 170 mm at the current of 400 A, but the component of the second order derivative of $B(r)$ contributes to the chromaticity as well as that of $\ell_{eff}(r)$. Comparing with the values of B''/B_0 and ℓ''_{eff}/ℓ_g shown in Table 6, the contribution of the former is much less than the latter. The value of B''/B_0 was expected as $0.056 \sim 0.070$ m^{-2} (Chapter 2) and was measured at $0.03 \sim 0.06$ m^{-2}, which agrees well.

5. Individuality

It was expected that the eight magnets would have slight different characteristics with each other. In the design stage, therefore, it was decided these magnets had correction coils of 600 AT which corresponds to 11 % of 55200 AT of main coil. The field strengths of eight magnets at I = 370 A and deviations from the average field are listed in Table 8. The gap height of each magnet is also given in the same table which is derived from averaging the measured values of ten points distributed in whole aperture.

On the other hand, effective lengths along the orbit at $\rho = 1.353$ m are obtained by the coefficient b_0 in Table 6. These results are given in Table 8 and are shown by histgram in Fig. 22. As obviously known from the figure, the required maximum correction ability is about 2.5×10^{-3}, whereas each magnet has a correction capability of $\pm 5 \times 10^{-3}$ and it covers well the requirement for the correction.

(6) Fields at off-median planes

Until now we discuss about the results in the median plane ($z = 0$), while the field distributions in the off-median planes ($z = \pm 15$ mm) were also measured. In the preceding analysis, planar effect12),13) of Hall-probe does not need to be considered because the measurement is executed on the median plane and the flux line is prependicular to the Hall-probe. The typical results in the planes of $z = \pm 15$ mm are shown in Fig.s 23, 24 and 25, where given are the fringing field, the effective length and the uniformity of inner field, respectively, with those in the median plane for comparison. These results show the differences of field properties among the three horizontal planes including the contribution of planner effect. We obtained the conculsion that there is no obvious differences in magnetic field characteristics between median and off-median planes.

5. Discussion

The effect of the eight bending magnets on the chromaticity is estimated as follows. The contribution of dipole magnets to the chromaticity is normally ignored for large rings, but it may not be adequate for rather small ones such as TARN. The chromaticity formula due to the dipole contribution are derived by A. Garren14) as

$$\xi_x \equiv \frac{d\nu_x}{d(\frac{\Delta p}{p})} = \frac{1}{4\pi\rho}\int [(-\frac{2}{\rho} - K\rho)\beta_x + (\frac{1}{\rho^2} + 3K + K'\rho)\beta_x\eta + \gamma_x\eta]ds \quad ,$$

$$\xi_z \equiv \frac{d\nu_z}{d(\frac{\Delta p}{p})} = \frac{1}{4\pi\rho}\int [K\rho\beta_z - (K + K'\rho)\beta_z\eta + \gamma_z\eta]ds \quad , \qquad (16)$$

where β and γ are Twiss parameters and η is the dispersion function. K and K' are given by

$$K = \frac{1}{B\rho}\frac{dB}{dx} \quad ,$$

$$K' = \frac{1}{B\rho}\frac{d^2B}{dx^2} \quad . \qquad (17)$$

Taking first order approximation, Twiss parameters and the dispersion function are assumed to be constant in the magnet and the relation (16) can be rewritten as

$$\xi_x = \frac{1}{4\pi\rho}\Big[\Big(\Big(-\frac{2}{\rho}+\frac{1}{\rho^2}\langle\eta\rangle\Big)\langle\beta_x\rangle+\langle\gamma_x\rangle\langle\eta\rangle\Big)\cdot I_0(x) + (-\rho+3\langle\eta\rangle)\,\langle\beta_x\rangle\cdot I_1(x)$$

$$+\ \rho\langle\beta_x\rangle\langle\eta\rangle\cdot I_2(x)\Big] \quad , \tag{18}$$

$$\xi_z = \frac{1}{4\pi\rho}\Big[\langle\gamma_z\rangle\langle\eta\rangle\cdot I_0(x) + (\rho-\langle\eta\rangle)\langle\beta_z\rangle\cdot I_1(x) - \rho\langle\beta_z\rangle\langle\eta\rangle\cdot I_2(x)\Big] \quad ,$$

where the bracket means the average value of each variable and I_0, I_1 and I_2 represent the following integrals,

$$I_0(x) = \frac{1}{B(x,\ 0)}\int B(x,\ s)\,ds = \ell_{eff}(x) \quad ,$$

$$I_1(x) \equiv \int K ds = \frac{1}{B(x,\ 0)\cdot\rho}\int \frac{dB(x,\ s)}{dx}\,ds$$

$$= \frac{1}{\rho}\,\frac{d\ell_{eff}(x)}{dx} + \frac{1}{B(x,\ 0)}\,\frac{dB(x,\ 0)}{dx}\,\frac{\ell_{eff}(x)}{\rho} \quad , \tag{19}$$

$$I_2(x) \equiv \int K' ds = \frac{1}{B(x,\ 0)\cdot\rho}\int \frac{d^2B(x,\ s)}{dx^2}\,ds$$

$$= \frac{1}{B(x,0)}\,\frac{d^2B(x,0)}{dx^2}\,\frac{\ell_{eff}(x)}{\rho} + 2\,\frac{1}{B(x,0)}\,\frac{dB(x,0)}{dx}\,\frac{1}{\rho}\,\frac{d\ell_{eff}(x)}{dx} + \frac{1}{\rho}\,\frac{d^2\ell_{eff}(x)}{dx^2} \quad .$$

In the present case, the numerical values are $\langle\eta\rangle = 1.3$ m, $\langle\beta_x\rangle = 3.7$ m, $\langle\beta_z\rangle = 2.0$ m, $\langle\gamma_x\rangle = 0.55$ and $\langle\gamma_z\rangle = 1.0$[15]. Substituting the values of B', B'', ℓ'_{eff}, ℓ''_{eff} in Table 9 into the above relations, total integrations of I_0, I_1 and I_2 throughout the ring are obtained as 8.57 m, 0.013 m^{-1} and -1.35 m^{-2}, respectively. In Table 9 the coefficients are obtained by fitting with second order polynominals, which means that higher order terms than the sextupole component are ignored. Therefore, the contributions of dipoles to chromaticities are estimated at

$$\xi_x = -1.59 \quad , \qquad \xi_z = 0.93 \quad .$$

These values are almost consistent with the measured values by the RF knock-out method$^{16)}$. It is expected at TARN that $\Delta p/p$ changes by the amount of 6.29 %$^{4)}$ when RF stacking is applied and ν-shifts in this case are

$$\begin{aligned} \Delta\nu_x &= \xi_x \cdot \frac{\Delta p}{p} = -0.10 \quad , \\ \Delta\nu_z &= \xi_z \cdot \frac{\Delta p}{p} = 0.06 \quad , \end{aligned} \tag{20}$$

respectively.

Acknowledgements

The authers would like to express their sincere thanks to Dr. Al. Garren at LBL for his instruction on the chromaticity formula.

Numerical calculation with the computer code TRIM was executed by HITAC 8800 at KEK and FACOM 230-75 at IPCR. Orbit calculation with the program SYNCH was executed by TOSBAC 3400 at INS.

They are indebted to Dr. N. Tokuda and the members in the study group of NUMATRON for their collaboration in the measurement of magnetic fields. They are also grateful to the members of the machine shop at INS for the construction of measuring apparatus, especially to Mr. H. Furuya for his skillful adjustment of the apparatus. One of them (T. Hattori) is grateful to Dr. S. Motonaga for his suggestions about the electronics system of a Hall-probe.

Thanks are also due to Profs. M. Sakai and K. Sugimoto for their continuous encouragement through the work, and to Mrs. M. Mamiya for her perseverence in typing within limited term.

References

1) A. Noda et al., "Lattice Structure and Magnet Design for the TEST RING", Proc. of the 2nd Symp. on Acc. Scie. & Tech. (1978) 83.

2) A. A. Garren and J. W. Eusebio, Lawrence Radiation Laboratory Report, UCID-10154 (1965).

3) G. Parzen, "Magnetic Fields for Transporting Charged Beams", BNL, ISA 76-13 (1976).

4) S. Yamada and T. Katayama, "Injection and Accumulation Method in the TARN", INS-NUMA-12 (1979).

5) A. M. Winslow, "Numerical Calculation of Static Magnetic Fields in an Irregular Triangle Mesh", UCRL-7784 (1964).

6) K. Endo, "Operational Manual of Two-Dimensional Magnetic Program TRIM", KEK-ACCELERATOR-2 (1974).

7) N. J. Diserens, "Futher Development of the Magnetostatic Computer Program TRIM at the Rutherford Laboratory", RHEL/R171 (1969).

8) W. Rogowski, "Die Electrische Festigkeit am Rande des Plattenkondensators", Archiv fur Elektrotechnik, 7 (1923) 1.

9) H. Kumagai, "On a Design of Wide Range Magnet for Cyclotron", Nucl. Inst. Meth. 6 (1960) 213.

10) M. Yoshizawa, "A Pulse Motor Controller", to be published by INS-NUMA.

11) S. Motonaga, private communication.

12) K. Amako et al., "Field Reconstruction for the KEK Large-Aperture-Spectrometer-Magnet TOKIWA", KEK-78-15 (1978).

13) C. Goldberg and R. E. Davis, "New Galvanomagnetic Effect", Phys. Rev. 94 (1954) 1121.

14) A. A. Garren, private communication.

15) Y. Hirao et al., "Test Accumulation Ring for NUMATRON Project - TARN - ", *INS-NUMA-10* (1979).

16) A. Noda et al., "Measurement of ν-values for TARN by the RF Knock-out Method" to be published soon by INS-NUMA.

Figure Captions

Fig. 1 Overall view of Test Accumulation Ring for NUMATRON (TARN).

Fig. 2 Structure of a normal cell. Q_F; focusing quadrupole, Q_D; defocusing quadrupole.

Fig. 3 Orbit characteristics in a period. (a) Beta and dispersion functions. (b) Alpha functions.

Fig. 4 Useful aperture requirement in bending magnet. The center of free space corresponds to the point at $\rho = 1333$ mm.

Fig. 5 Distribution of flux density in radial direction along the center line at $z = 0$. (a) From the inside yoke ($r = 63$ cm) to the outside one ($r = 194$ cm), with cross sectional view of the magnet. (b) Fine structure in the gap region ($122.4\ \mathrm{cm} \le r \le 148.2\ \mathrm{cm}$). Solid line; calculation of TRIM, dashed line; typical measured data.

Fig. 6 B-H characteristics of low carbon steel we used.

Fig. 7 Edge shape of the magnet and Rogowski's curve, with co-ordinate system.

Fig. 8 Drawings of the dipole magnet. (a) Plan view. (b) Cross sectional view.

Fig. 9 Total view of the manufactured magnet.

Fig. 10 System constitution. (a) Block diagram of automatic measuring system. (b) Relations among CPU, peripherals and devices. (D.V.M = digital voltmeter).

Fig. 11 Flow chart of measuring procedure. (see Fig. 12 about (x, y) co-ordinates system).

Fig. 12 Relative position of Hall-probe driving apparatus to a magnet and mapped area normally used, together with various co-ordinates.

Fig. 13 (a) Overall view of measurement. (b) Magnified view of Hall-probe driving apparatus.

Fig. 14 Hall-probe stabilizing circuits. (a) Temperature control: dashed line is Hall-probe container box and two resistances in it are heater and thermistor (framed). (b) D.C. current stabilizer contained in a oven.

Fig. 15 Fluctuation of measuring system including Hall-probe and digital voltmeter (D.V.M.). White circle (°) and solid circle (·) represent maximum and minimum values in each 5 minutes, respectively.

Fig. 16 Calibration curve of Hall probe [$B(V_{Hall})$]. B/V_{Hall} vs. V_{Hall} represents its deviation from linearity.

Fig. 17 Excitation curve of a magnet. The dashed line is its initial inclination and the solid line shows its deviation from linearity.

Fig. 18 Hysteresis characteristics. The solid and dashed lines correspond to the cases of current increasing and decreasing, respectively.

Fig. 19 Fringing field normalized by the central field strength. The case of no field clamp is shown with the dash-dotted line at I = 400 A.

Fig. 20 Radial dependence of the difference of actual magnetic length from the geometrical one. The dash-dotted line shows the case of no field clamp at I = 400 A. The origin of abscissa is the same as Fig. 20.

Fig. 22 Difference of individual characteristics among 8 magnets. Deviations from the average values of field strength and of effective length are represented by the height of white and solid bars, respectively.

Fig. 23 Z-dependance of fringing field along the central orbit at I = 400 A.

Fig. 24 Z-dependence of radial distribution of inner field strength at I = 400 A.

Fig. 25 Z-dependence of radial distribution of effective length at I = 400 A.

Table Captions

Table 1 Useful aperture requirement in bending magnet.

Table 2 Chemical components of impurities and occupied percentage of them in low carbon steel we used.

Table 3 Specifications of the dipole magnet.

Table 4 Fitted coefficients of excitation curve B(i). ($0 \leq i \leq 400$ A)

Table 5 Fitted coefficients of fringing field $B_{fring}(s)/B_0$. (-120 mm $\leq s \leq 120$ mm)

Table 6 Fitted coefficients of effective length $\Delta\ell_{eff}(r)/\ell_g(0)$. ($-85$ mm $\leq r \leq 85$ mm)

Table 7 Fitted coefficients of inner field $\Delta B(r)/B_0$. (-95 mm $\leq r \leq 105$ mm)

Table 8 Deviations of gap height (d), field strength and effective length at $I = 370$ A from the average values.

Table 9 Fitted coefficients till sextupole component ($n = 2$) of $\Delta\ell_{eff}(r)/\ell_g(0)$ and $\Delta B(r)/B_0$.

	Horizontal Direction	Vertical Direction
Closed Orbit Distortion	11.2 mm	7.8 mm
Betatron Oscillation	16.3	5.0
Momentum Spread	40.5	—
Clearance	21.8	9.7
SUM (Half Size)	109.0 mm*	22.5 mm

* It is not a simple sum of the values listed. The situation of this value is illustrated in Fig. 4.

Table 1

C	Si	Mn	P	S
0.04	TR*	0.33	0.015	0.007

(%)

* Only trace is detected.

Table 2

Dipole Magnet (Window-Frame type)

Width of the Aperture	258 mm
Gap Height	70 mm
Radius of Curvature*	1,333 mm
Mechanical Length	1,047 mm
Bending Angle	45°
Maximum Field	9 kG
Main Coil	
Maximum Ampere Turns	55200 AT
Number of Turns	138 Turns
Maximum Current	400 A
Maximum Current Density	5.38 A/mm^2
Resistance of the Coil**	0.147Ω
Maximum Power Dissipation	23.5 kW
Space Factor	0.475
Pressure Drop of Cooling Water	2.07 kg/cm^2
Flowing Rate of Cooling Water	13.548 ℓ/min
Correction Coil	
Maximum Ampere Turns	600 AT
Number of Turns	4 Turns
Maximum Current	150 A
Maximum Current Density	5.01 A/mm^2
Resistance of the Coil**	0.01354Ω
Maximum Power Dissipation	0.305 kW

* At the center of useful aperture

** The values at 50°C

Table 3

Magnet No.	A_0	A_1	A_2	A_3	A_4	A_5
	$\times10^{-1}$	$\times10^{-1}$	$\times10^{-4}$	$\times10^{-6}$	$\times10^{-9}$	$\times10^{-13}$
1	-.36672	.26483	-.23292	.10653	-.17699	- .01041
2	-.25661	.25837	-.15501	.06880	-.09570	- .65184
3	-.45977	.26822	-.27347	.12813	-.23028	.48429
4	-.90564	.28555	-.46542	.21194	-.38545	1.49434
5	-.57537	.27238	-.32011	.14663	-.25557	.52656
6*	-.10942	.25459	-.10159	.03241	.01058	-1.72366
7**	-.37624	.26595	-.24875	.11306	-.11850	———
8	-.18914	.25811	-.13743	.04990	-.02965	-1.37580

$B(i) = \sum_{n=0}^{5} A_n i^n$, B : kG , i : Ampère

The number of fitted points is 16 except * (14) and ** (8).

Table 4

z (mm)	x (mm)	B_0(kGauss)	a_0	$a_1(m^{-1})$	$a_2(m^{-2})$	$a_3(m^{-3})$	$a_4(m^{-4})$	$a_5(m^{-5})$	$a_6(m^{-6})$	$a_7(m^{-7})$
				$\times 10^1$	$\times 10^2$	$\times 10^4$	$\times 10^5$	$\times 10^7$	$\times 10^8$	$\times 10^{10}$
0.0	0.0	4.8957	.48590	.87264	-.14678	-.36140	.35935	.31108	-.46421	-.21953
		8.2742	.49626	.84850	-.08494	-.36313	.26676	.34094	-.37564	-.27237
		8.7046	.49729	.84201	-.06258	-.36491	.23748	.35225	-.34979	-.29096
		9.0973	.50401	.83268	-.05644	-.36376	.22214	.35820	-.33564	-.30243
-15.0			.50546	.88477	-.11795	-.42406	.38095	.43519	-.56805	-.36645
15.0			.50024	.86945	-.08049	-.40726	.31550	.41516	-.48275	-.35094
0.0	-115.0		.49982	.85657	-.14575	-.35731	.37754	.29927	-.50568	-.18946
	-85.0		.50247	.83763	-.05921	-.36803	.22848	.36402	-.34332	-.30865
	-55.0		.50365	.83353	-.05616	-.36454	.22210	.35936	-.33588	-.30364
	-25.0		.50391	.83276	-.05606	-.36374	.22172	.33391	-.33521	-.30170
	- 5.0		.50406	.83260	-.05638	-.36356	.22183	.35762	-.33513	-.30144
	25.0		.50405	.83279	-.05712	-.36377	.22306	.35794	-.33664	-.30175
	55.0		.50390	.83336	-.05722	-.36431	.22305	.35893	-.33666	-.30311
	85.0		.50298	.83728	-.06046	-.36778	.22901	.36354	-.34339	-.30782

$$a_n = \frac{1}{B_0}\left(\frac{d^n B_{fring}(s)}{ds^n}\right)_{s=0}$$

Table 5

Magnet 1) No.		b_0	$b_1(m^{-1})$	$b_2(m^{-2})$	$b_3(m^{-3})$	$b_4(m^{-4})$
		$\times 10^{-2}$	$\times 10^{-3}$	$\times 10^{-1}$		$\times 10^{3}$
1		.76343	.44741	-.97412	.15737	-.25308
2		.83538	.56410	-1.03794	.24690	-.28096
3		.83032	.65418	-.94064	.48592	-.32938
4		.89455	.46701	-.93535	.51233	-.30103
5		.86295	.17897	-.83628	.72998	-.33086
6		.78543	-.33275	-.74270	.19009	-.32055
7		.78717	1.03923	-.82991	-.14663	-.30660
8		.87799	1.17545	-.93303	.19613	-.31270
Z (mm)	I (A)					
		$\times 10^{-2}$	$\times 10^{-3}$	$\times 10^{-1}$		$\times 10^{3}$
	200 2)	-.19383	.23022	-.17866	.01547	-.05978
0.0	350 2)	.19784	.29052	-.32675	.06416	-.11459
	375 2)	.29184	.15823	-.23831	.03677	-.15056
15.0	400	.90846	.27277	-1.02342	1.02014	-.15598
-15.0		.83850	-.92679	-1.06528	-1.66762	-.21769

$$b_0 = \frac{\ell_{eff}(0)}{\ell_g(0)} - 1 , \qquad b_n = \frac{1}{\ell_g(0)}\left(\frac{d^{(n)}\ell_{eff}(r)}{dr^{(n)}}\right)_{r=0}$$

1) The values at I = 400 A and z = 0.0 mm are listed.

2) The values include the contribution form only one edge.

Table 6

Magnet 1) No.	c_0	$c_1(m^{-1})$	$c_2(m^{-2})$	$c_3(m^{-3})$	$c_4(m^{-4})$
	$\times 10^{-3}$	$\times 10^{-3}$	$\times 10^{-1}$		$\times 10^{2}$
1	-.22054	.41670	.25918	.62709	.06532
2	.23259	.78761	.57805	.23723	-.04419
3	-.09146	1.17078	.37990	.17050	.22781
4	.15128	1.13255	.52964	.15455	-.08850
5	-.22898	.47093	.28691	-.00595	.12431
6	.18049	.85028	.41697	.26066	.15186
7	-.16540	.86406	.40043	.41146	.35619
8	.14949	.87034	.29548	-.02164	.13060
Z (mm) I (A)					
	$\times 10^{-3}$	$\times 10^{-3}$	$\times 10^{-1}$		$\times 10^{2}$
200	-.26766	1.04210	.07333	-.28949	.56638
0.0 350	-.00930	.79289	.06865	-.25111	.19717
375	-.11285	.79446	.31900	-.33790	.03774
15.0 400	-.24050	.97212	.33132	-.53769	-.13116
-15.0	-.13635	.86828	.33661	.27844	.26159

1) The values at I = 400 A and z = 0.0 mm are listed.

$$C_0 = \frac{B(0)}{B_0} - 1 \quad , \qquad C_n = \frac{1}{B_0}\left(\frac{d^nB(r)}{dr^n}\right)_{r=0}$$

Table 7

Magnet No. average	$(\Delta B_i/\bar{B})_{I=370A}$ $\bar{B}$ = 8.6353 kG	$d_i/\bar{d}$ $\bar{d}$ = 70.061 mm	$(\Delta \ell_i/\bar{\ell}_{eff})_{\rho=1353mm}$ $\bar{\ell}_{eff}$ = 1071.5 mm
	$\times 10^{-3}$	$\times 10^{-4}$	$\times 10^{-3}$
1	-.7527	2.08	-.6424
2	.7527	2.37	.0816
3	-.5559	2.37	.0419
4	-.1853	1.27	.6667
5	-1.3896	2.30	.3692
6	.5559	2.16	-.4143
7	-.4632	1.73	-.3944
8	2.0381	-14.83	.5080

Table 8

Magnet No.	b_0	$b_1(m^{-1})$	$b_2(m^{-2})$	$c_1(m^{-1})$	$c_2(m^{-2})$
	$\times 10^{-2}$	$\times 10^{-2}$		$\times 10^{-2}$	$\times 10^{-1}$
1	.76918	.31358	-.24188	.09991	.29965
2	.84176	.07627	-.26418	.10287	.54957
3	.83781	.10450	-.28209	.13534	.55138
4	.90016	.08054	-.24814	.12770	.50384
5	.87046	.07660	-.27250	.04688	.37773
6	.79271	-.01799	-.25725	.10945	.51502
7	.79414	.09213	-.25801	.10751	.60638
8	.88509	.13332	-.27180	.08500	.38270

At I = 400 A and on the median plane (z = 0)

The meanings of b_n, c_n are the same as that of Tables 6 and 7.

Table 9

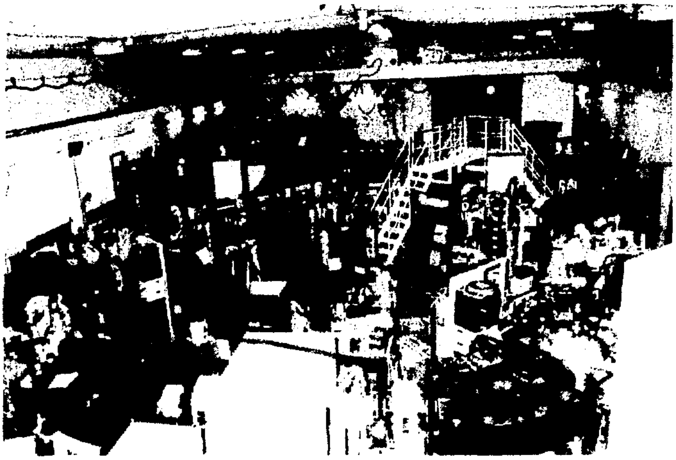

Fig. 1

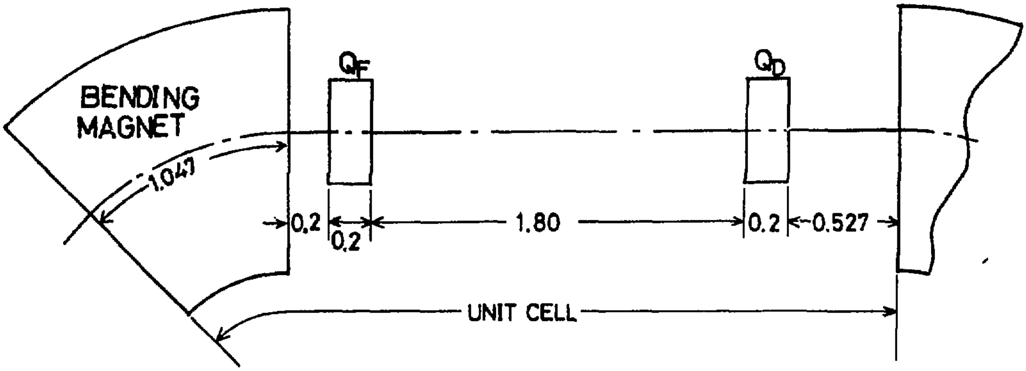

Fig. 2

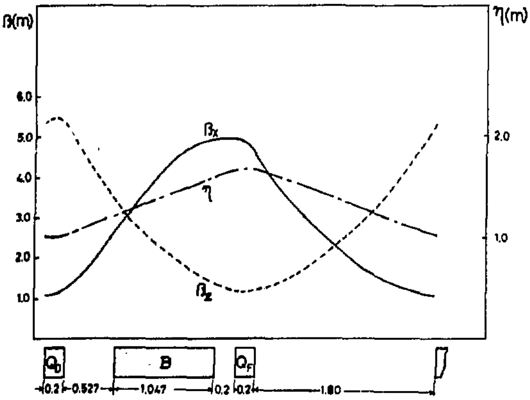

Fig. 3 (a)

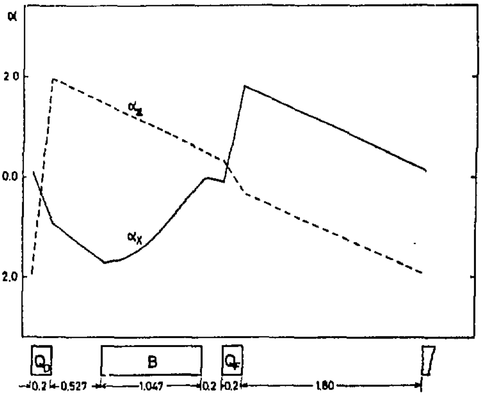

Fig. 3 (b)

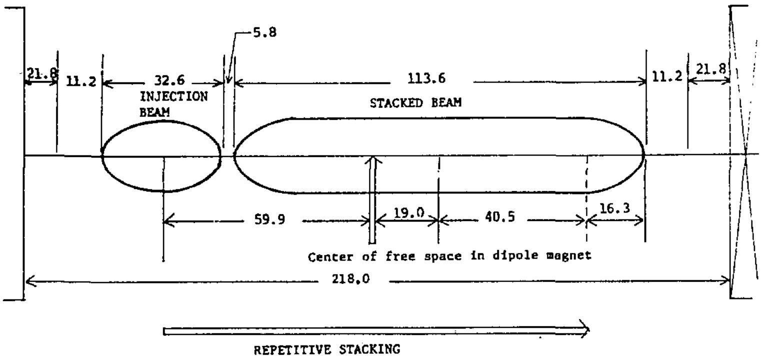

USEFUL APERTURE REQUIREMENT

Fig. 4

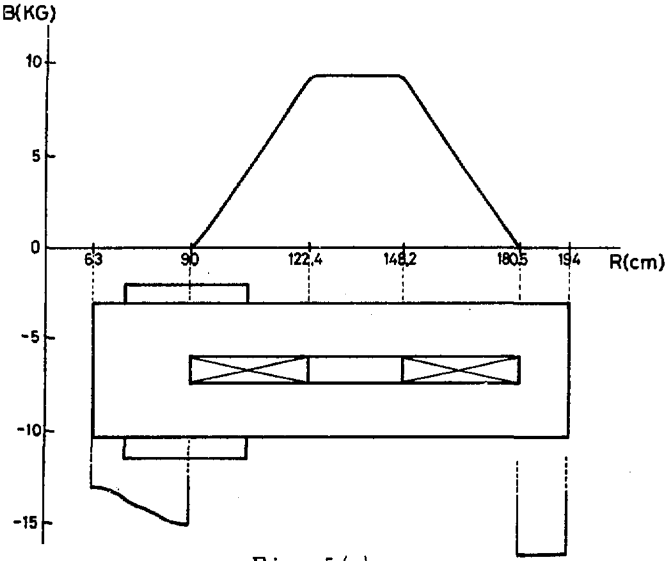

Fig. 5 (a)

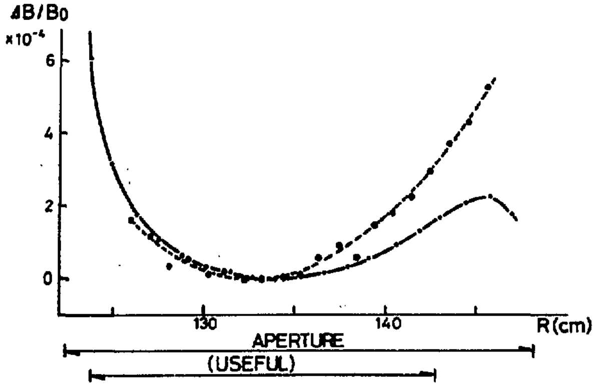

Fig. 5 (b)

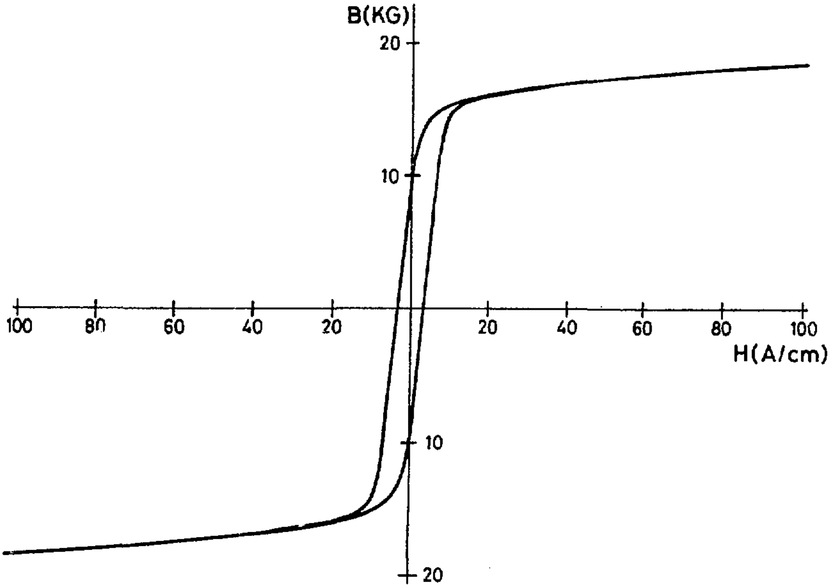
B(KG)
20
10
10
20
100
80
60
40
20
20
40
60
80
100
H(A/cm)

Fig. 6

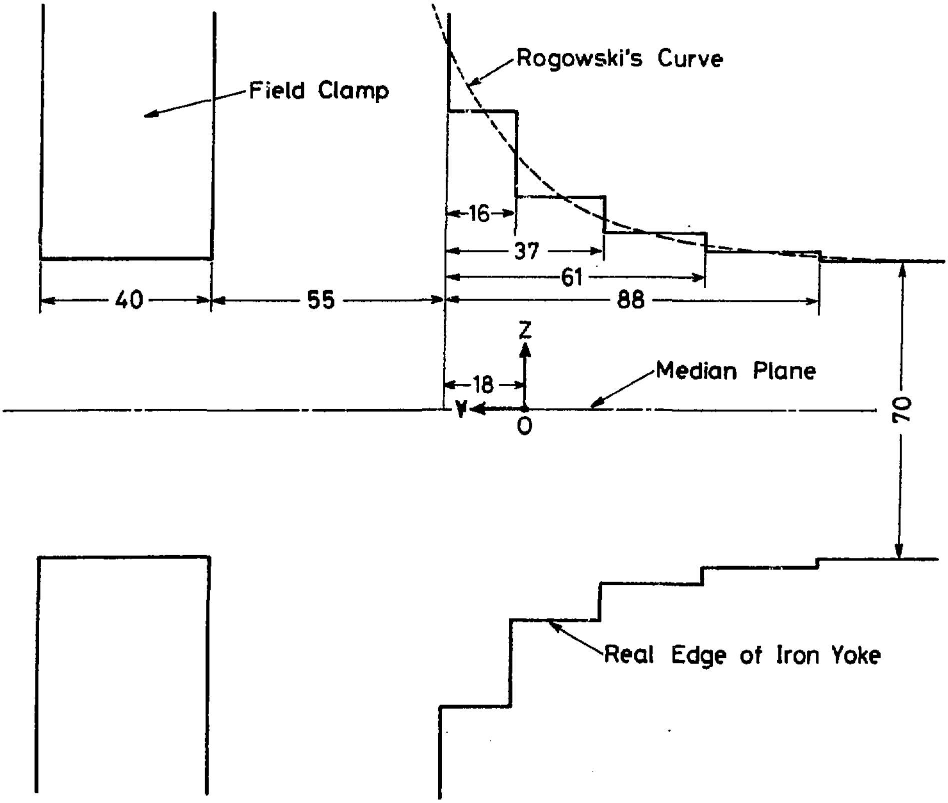
Field Clamp
Rogowski's Curve
16
37
61
88
40
55
Z
18
Y
O
Median Plane
70
Real Edge of Iron Yoke

Fig. 7

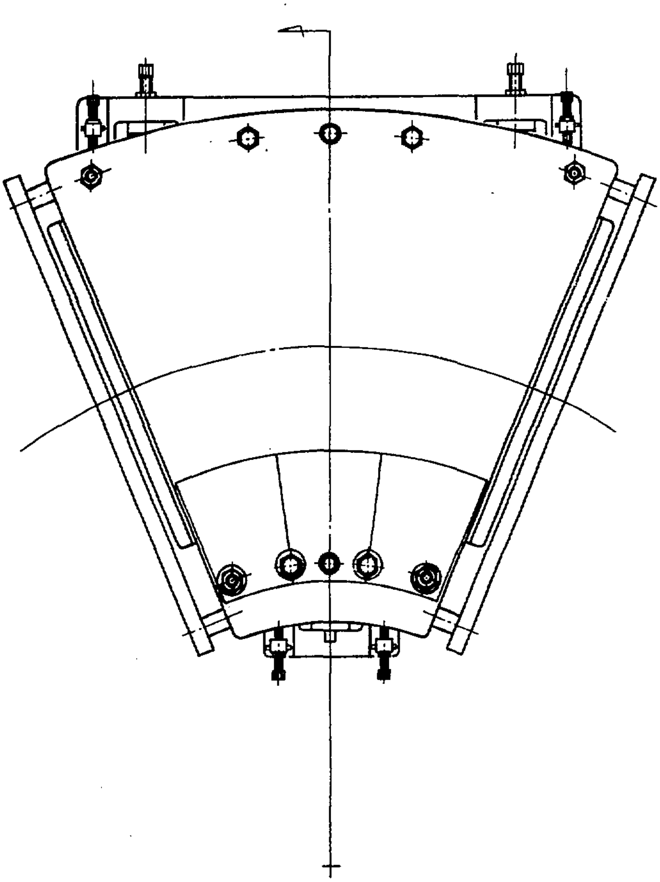

Fig. 8(a)

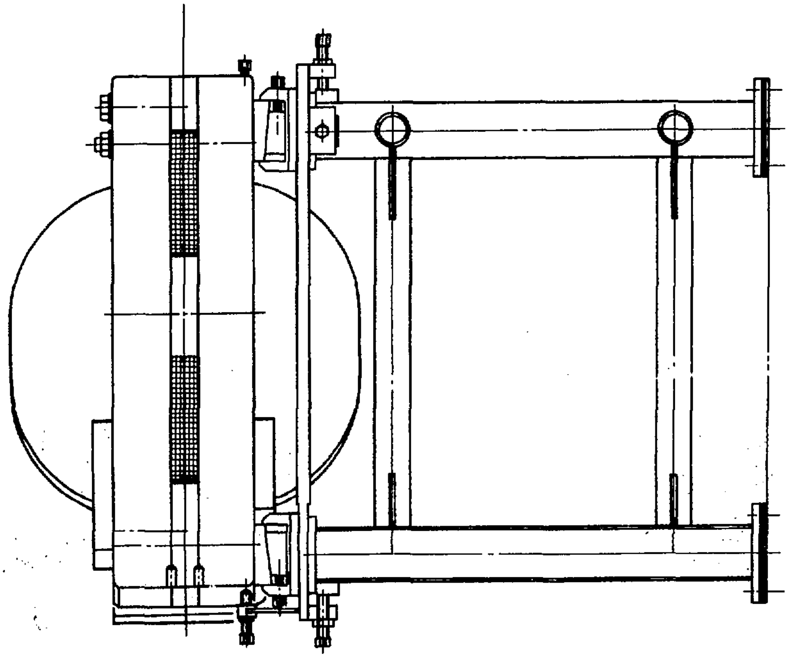

Fig. 8(b)

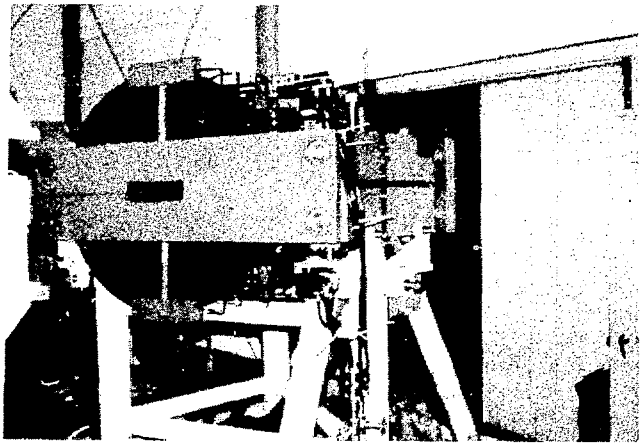

Fig. 9

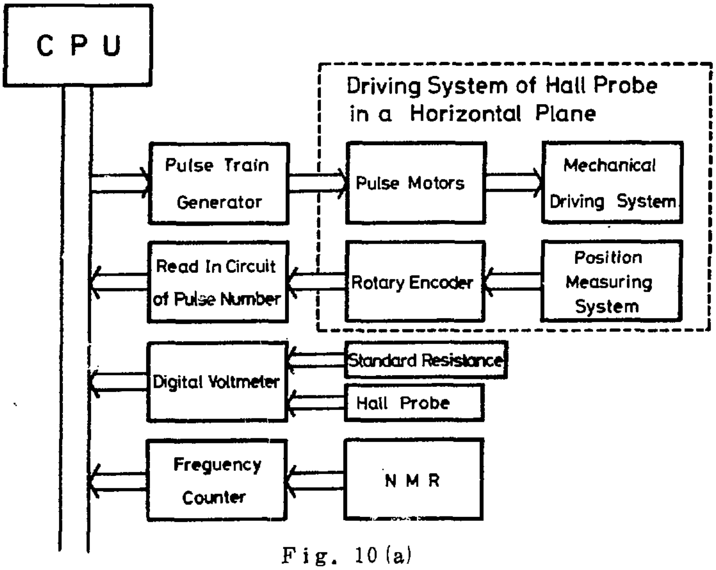

Fig. 10(a)

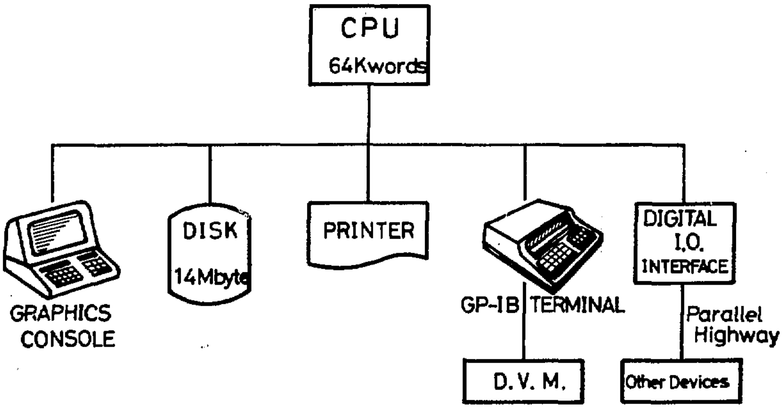

Fig. 10(b)

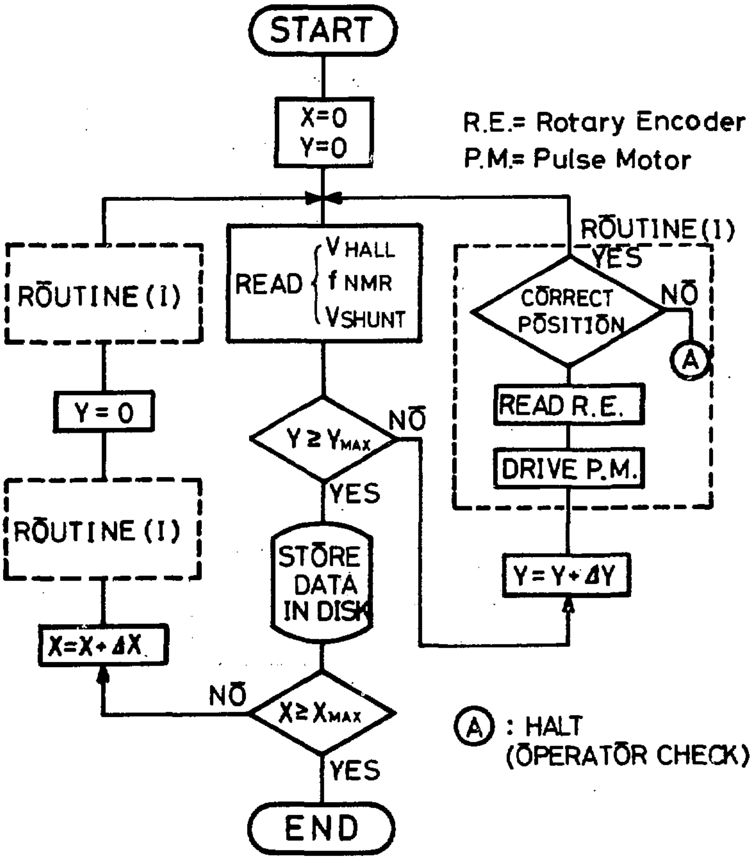
START
X=0
Y=0
R.E.= Rotary Encoder
P.M.= Pulse Motor
ROUTINE(I)
READ
V HALL
f NMR
VSHUNT
ROUTINE(I)
YES
CORRECT POSITION
NO
A
READ R.E.
DRIVE P.M.
Y=0
Y ≥ YMAX
NO
YES
ROUTINE (I)
STORE DATA IN DISK
Y=Y+ΔY
X=X+ΔX
NO
X≥XMAX
YES
END
A : HALT
(OPERATOR CHECK)

Fig. 11

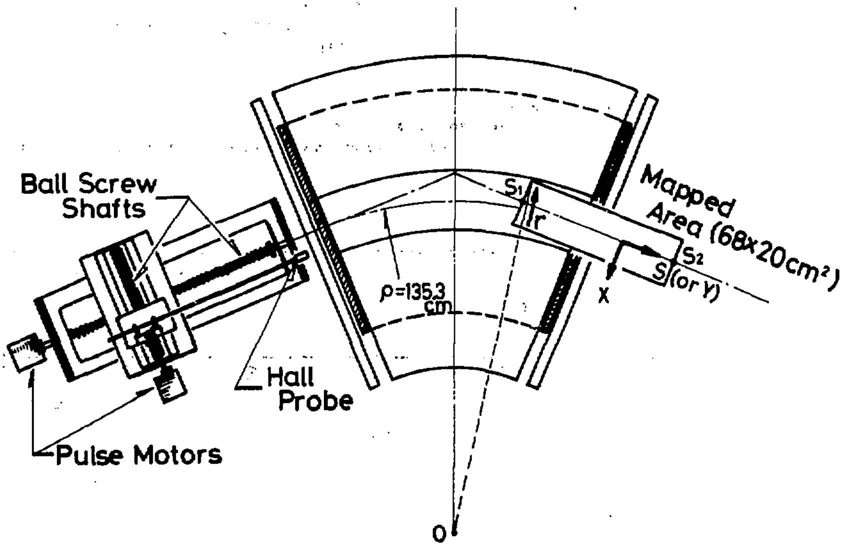
Ball Screw
Shafts
Mapped
Area (68×20cm²)
S1
r
S2
S (or Y)
X
ρ=135.3 cm
Hall
Probe
Pulse Motors
O

Fig. 12

Fig. 13 (a)

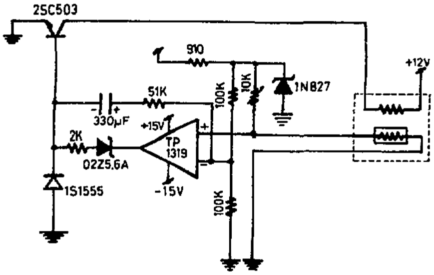

Fig. 14 (a)

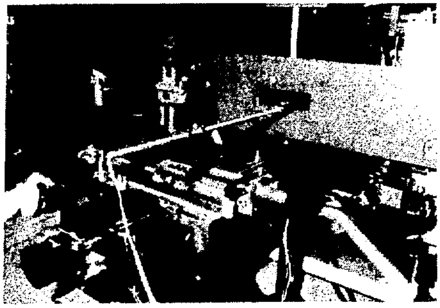

Fig. 13 (b)

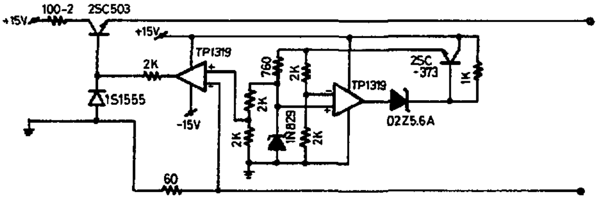

Fig. 14 (b)

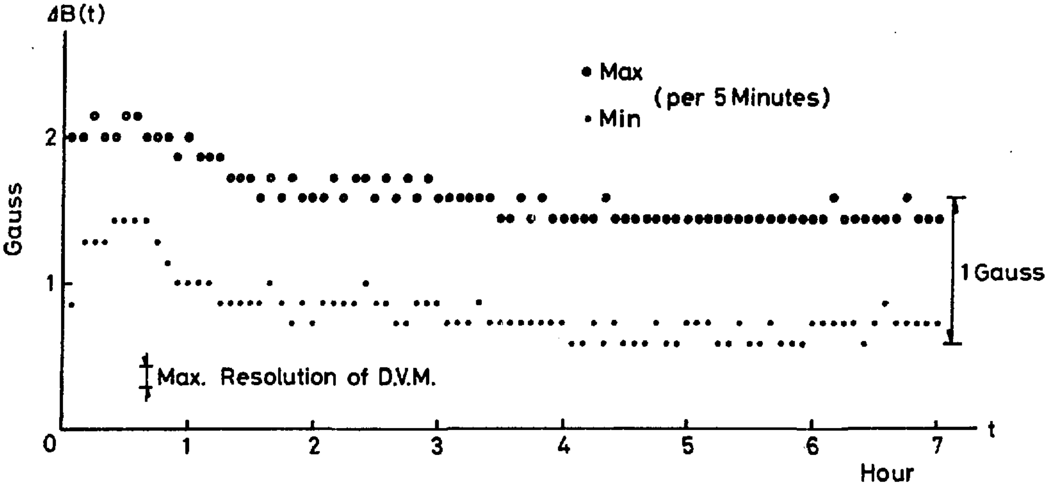

Fig. 15

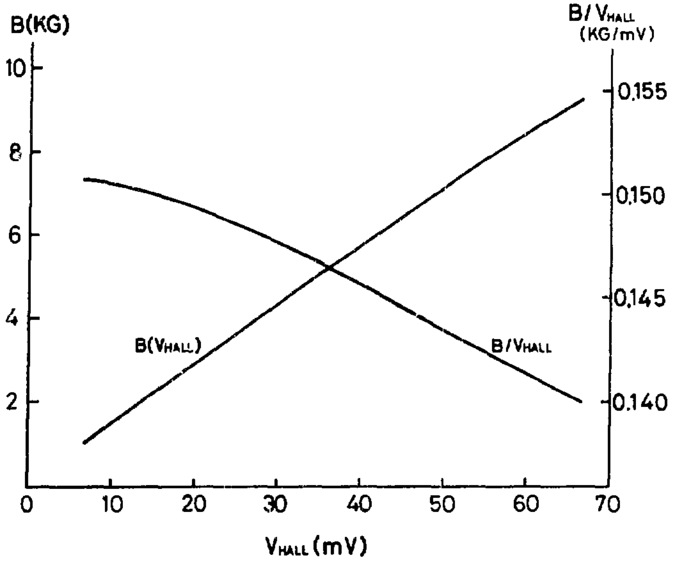
B(KG)
B/V_HALL (KG/mV)
10
8
6
4
2
0.155
0.150
0.145
0.140
B(V_HALL)
B/V_HALL
0
10
20
30
40
50
60
70
V_HALL (mV)

Fig. 16

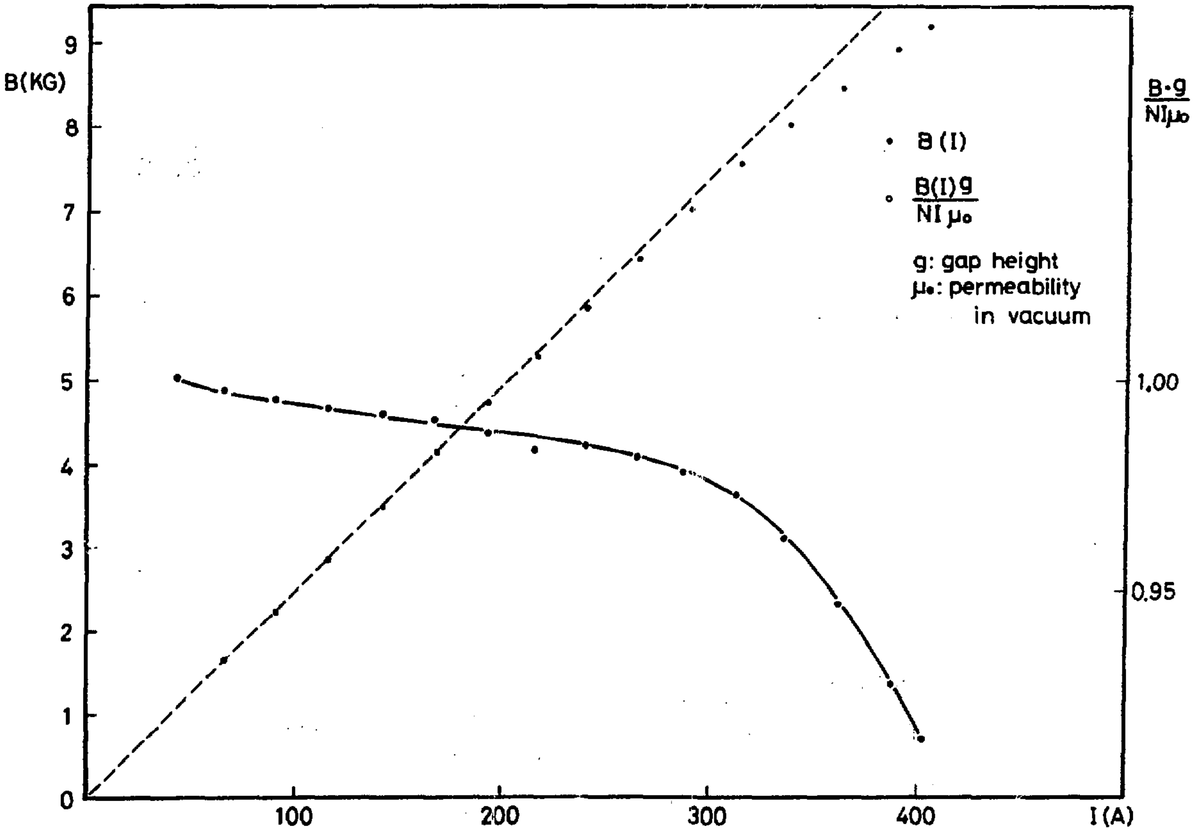
B(KG)
9
8
7
6
5
4
3
2
1
0
B·g / NIμ₀
1.00
0.95
• B (I)
∘ B(I)g / NI μ₀
g: gap height
μ₀: permeability in vacuum
100
200
300
400
I (A)

Fig. 17

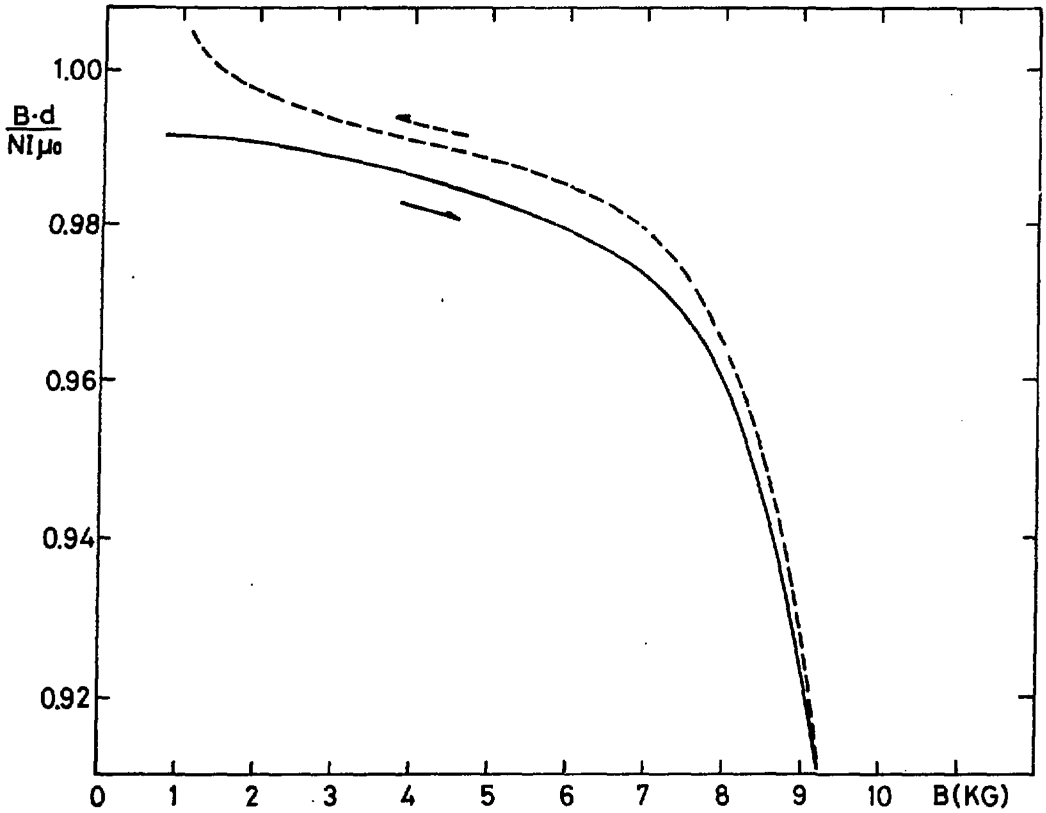
$\frac{B \cdot d}{NI\mu_0}$
1.00
0.98
0.96
0.94
0.92
0
1
2
3
4
5
6
7
8
9
10
B(KG)

Fig. 18

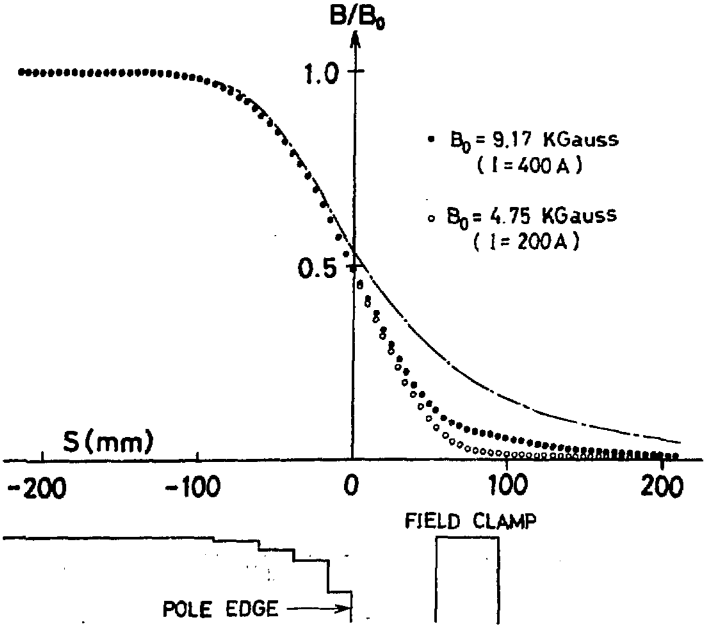
B/B_0
1.0
0.5
● B_0 = 9.17 KGauss
(I = 400 A)
○ B_0 = 4.75 KGauss
(I = 200 A)
S (mm)
-200
-100
0
100
200
FIELD CLAMP
POLE EDGE

Fig. 19

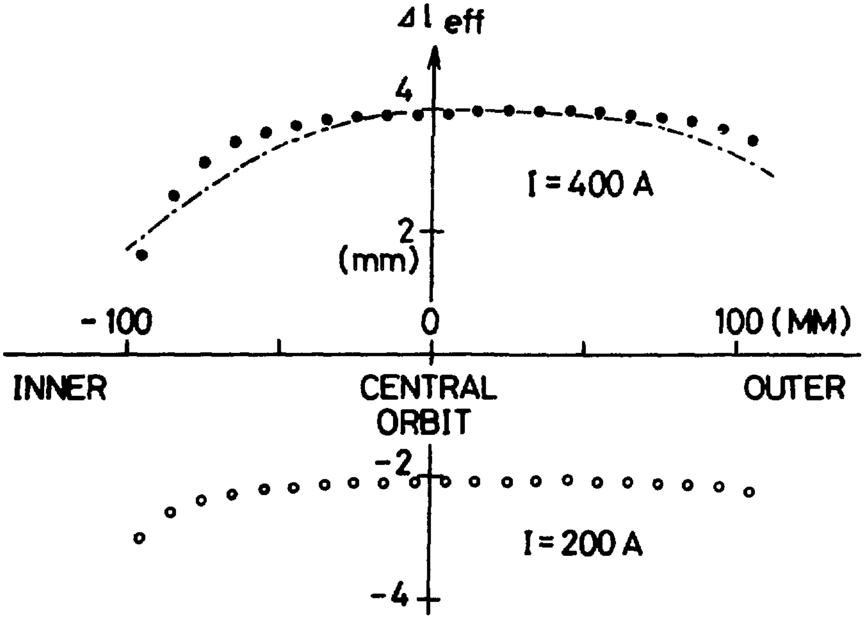
Δl eff
4
2
(mm)
I = 400 A
-100
0
100 (MM)
INNER
CENTRAL ORBIT
OUTER
-2
I = 200 A
-4

Fig. 20

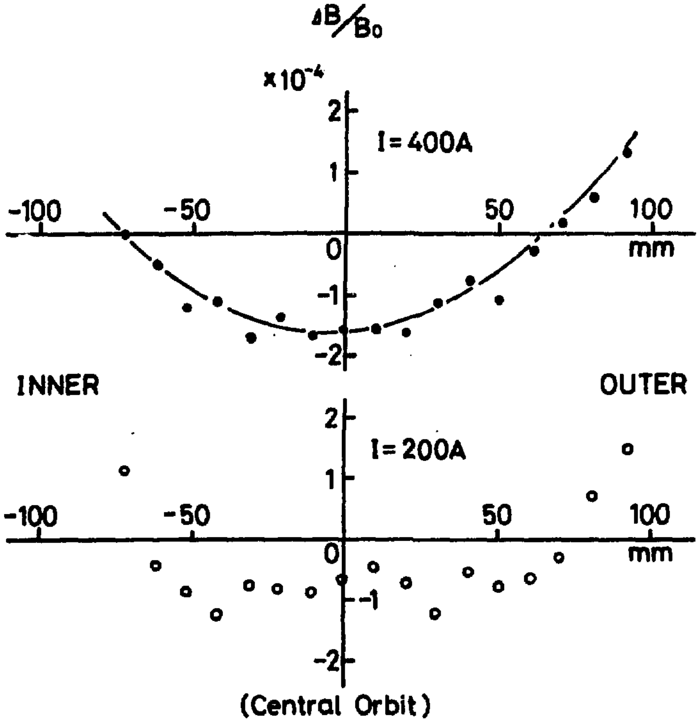
ΔB/B0
×10^-4
2
1
0
-1
-2
I = 400A
-100
-50
50
100
mm
INNER
OUTER
I = 200A
(Central Orbit)

Fig. 21

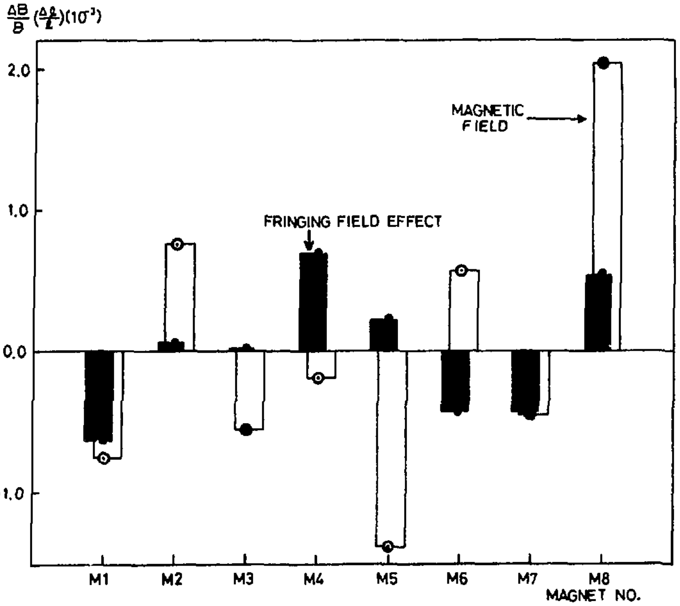
ΔB/B (Δℓ/ℓ)(10⁻³)
2.0
1.0
0.0
-1.0
MAGNETIC FIELD
FRINGING FIELD EFFECT
M1
M2
M3
M4
M5
M6
M7
M8
MAGNET NO.

Fig. 22

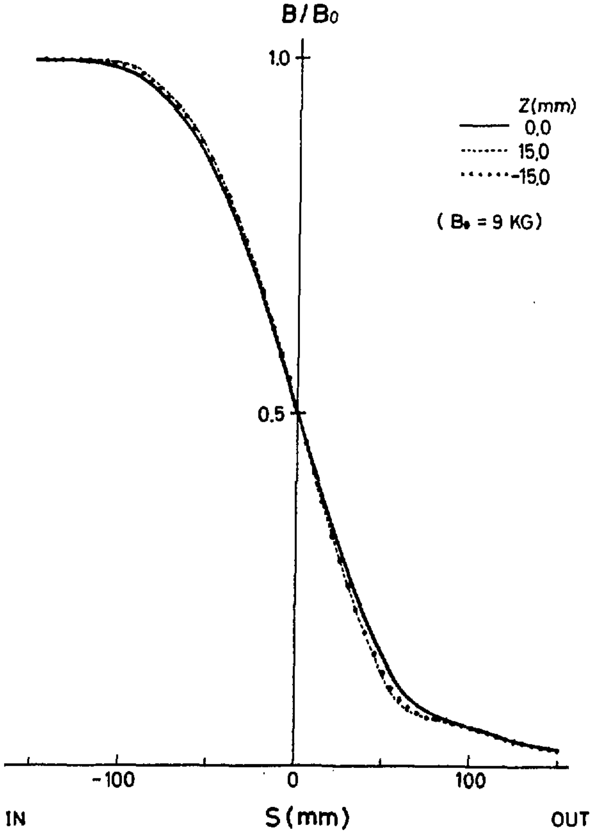
B/B₀
1.0
0.5
Z(mm)
0.0
15.0
-15.0
(B₀ = 9 KG)
-100
0
100
IN
S(mm)
OUT

Fig. 23

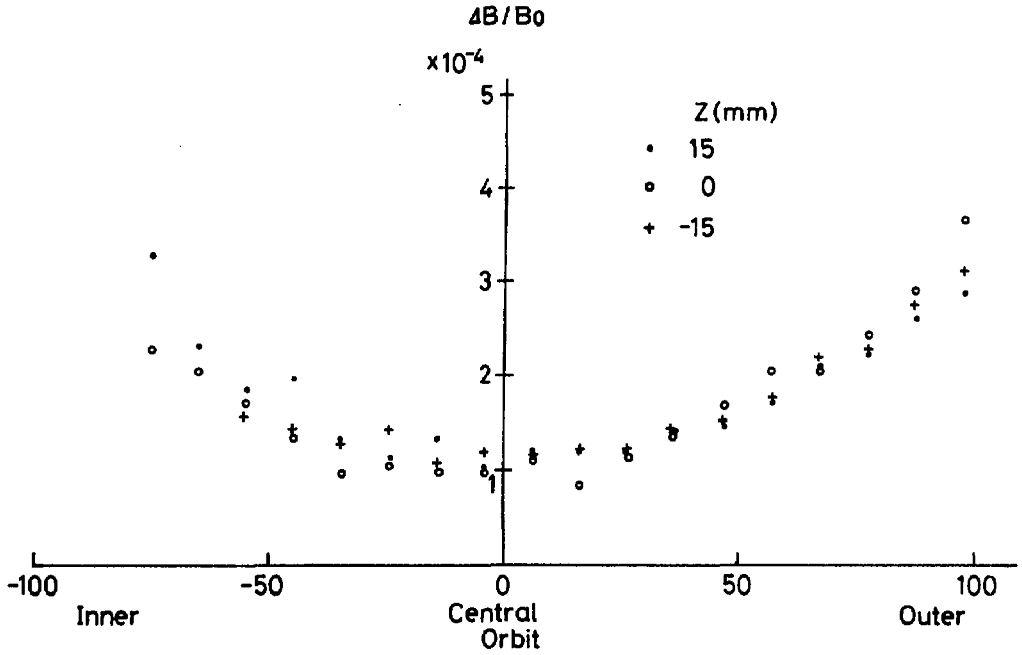
ΔB/Bo
x10^-4
5
4
3
2
1
Z(mm)
• 15
o 0
+ -15
-100
-50
0
50
100
Inner
Central
Orbit
Outer

Fig. 24

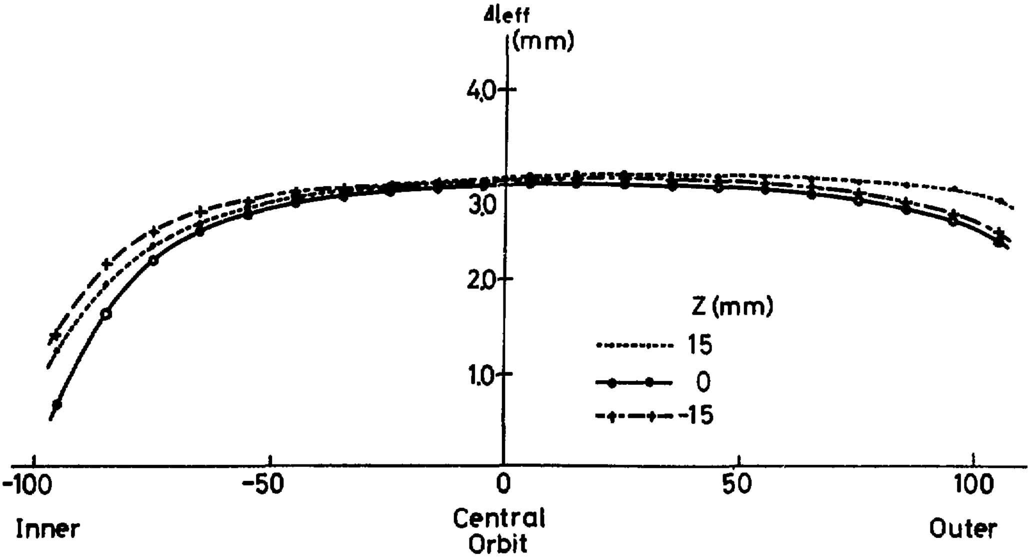
Δleff
(mm)
4.0
3.0
2.0
1.0
Z(mm)
15
0
-15
-100
-50
0
50
100
Inner
Central
Orbit
Outer

Fig. 25